Online terrain estimation for autonomous vehicles on deformable terrains *

James Dallas[a], Kshitij Jain[a], Zheng Dong[a], Leonid Sapronov[b], Michael P. Cole[c], Paramsothy Jayakumar[c], Tulga Ersal[a,*]

*This work was funded by U.S. Department of Defense under the prime contract number W56HZV-17-C-0005. DISTRIBUTION STATEMENT A. Approved for public release; distribution unlimited. OPSEC #2942.

*Corresponding author: tersal@umich.edu

Online terrain estimation for autonomous vehicles on deformable terrains

James Dallas[a], Kshitij Jain[a], Zheng Dong[a], Leonid Sapronov[b], Michael P. Cole[c], Paramsothy Jayakumar[c], Tulga Ersal[a,*]

[a] *J. Dallas, K. Jain, Z. Dong, and T. Ersal are with the Department of Mechanical Engineering, University of Michigan, 1231 Beal Ave, Ann Arbor, MI 48109, USA.*

[b] *Leonid Sapronov is with Robotic Research, 555 Quince Orchard Road, Suite 300, Gaithersburg, MD 20878, USA.*

[c] *M.P. Cole and P. Jayakumar are with the U.S. Army Ground Vehicle Systems Center, 6501 E Eleven Mile Rd, Warren, MI 48397, USA.*

Abstract

In this work, a terrain estimation framework is developed for autonomous vehicles operating on deformable terrains. Previous work in this area usually relies on steady state tire operation, linearized classical terramechanics models, or on computationally expensive algorithms that are not suitable for real-time estimation. To address these shortcomings, this work develops a reduced-order nonlinear terramechanics model as a surrogate of the Soil Contact Model (SCM) through extending a state-of-the-art Bekker model to account for additional dynamic effects. It is shown that this reduced-order surrogate model is able to accurately replicate the forces predicted by the SCM while reducing the computation cost by an order of magnitude. This surrogate model is then utilized in a unscented Kalman filter to estimate the sinkage exponent. Simulations suggest this parameter can be estimated within 4% of its true value for clay and sandy loam terrains. It is also shown in simulation and experiment that utilizing this estimated parameter can reduce the prediction errors of the future vehicle states by orders of magnitude, which could assist with achieving more robust model-predictive autonomous navigation strategies.

Keywords: Terramechanics, parameter estimation, wheeled vehicles, deformable terrain, control, Kalman Filter

☆This work was funded by U.S. Department of Defense under the prime contract number W56HZV-17-C-0005. DISTRIBUTION STATEMENT A. Approved for public release; distribution unlimited. OPSEC #2942.

*Corresponding author: tersal@umich.edu

1. Introduction

Autonomous ground vehicles (AGVs) have drawn interest for military applications to perform tasks, such as supply transport, in unsafe environments that could pose a threat to human operators (Iagnemma and Dubowsky, 2002). Three considerations about military AGVs are important to motivate this work. First, military vehicles often need to operate off-road on deformable terrains, where the vehicle's mobility is dependent on the highly nonlinear tire forces generated at the tire-terrain interface (Taheri et al., 2015). Second, increasing the mobility of military AGVs is a critical need (Liu et al., 2017). Third, state-of-the-art approaches to navigate such vehicles typically rely on model dependent architectures, such as Model Predictive Control (MPC) (Liu et al., 2017, 2018). Therefore, when the AGVs are operated on deformable terrains, a more accurate knowledge of the terrain parameters becomes a critical enabler to maximize the mobility of the AGVs.

Much research has been performed in developing terramechanics models for off-road applications, which can be divided into empirical models, physics-based models, semi-empirical models (Taheri et al., 2015). Empirical model are the simplest; however, such models do not generalize well beyond the experimental test conditions used for their development. On the other hand, physics-based finite and discrete element models have proven to be of the highest fidelity, but the large computational efforts required renders them infeasible for real-time tire force prediction, thus limiting their applicability for use in AGVs and real-time terrain estimation (Taheri et al., 2015). More promising candidates, and perhaps the most widely used, for real-time tire force prediction on deformable terrains are the semi-empirical models based upon the classical terramechanics theory developed by Bekker, including the Soil Contact Model (Gallina et al., 2014; Ishigami et al., 2007; Smith, 2014; Guo, 2016). In these models, the tire is typically assumed rigid and the deformation is assumed to occur only in the terrain (Smith, 2014). To model the complex tire-terrain interactions, these terramechanics models rely on knowledge of terrain-specific parameters such as cohesion, internal friction angle, or sinkage exponent. During vehicle operation, these parameters may not be explicitly known or may be varying due to non-uniform terrains. Therefore, real-time terrain estimation is necessary in AGVs to improve the accuracy of the terramechanics models online and generate better informed control commands. Having this capability would also provide insight into traversability of terrains, such that path planning algorithms can reroute the vehicle to avoid regions where loss of mobility or excessive power consumption is likely to occur (Iagnemma, 2006).

Researchers have already recognized this need and a limited number of results are available in the literature. In particular, in (Gallina et al., 2014, 2016), a Bayesian procedure is utilized for terrain parameter identification, but making this approach work online is subject to future research. Other researchers have proposed an online algorithm for estimating soil cohesion and internal friction angle utilizing a linear least-squares estimator for a rover (Iagnemma and Dubowsky, 2002; Iagnemma et al., 2004). The algorithm relies on simplifying classical terramechanics equations through linear approximations to increase computational efficiency and subjects the rover to periodic high and low speed traverses (Iagnemma and Dubowsky, 2002). Similarly, in (Ding et al., 2015), multiple terrain parameters are estimated through least squares curve fitting with promising results for a sand-like terrain. Due to large computation times in the Bekker-based model, on the order of 10 s to estimate the parameter, the model is linearized. Multiple linearized models are analyzed which take on the order of 15 ms to hundreds of ms depending on model simplicity, sacrificing estimation accuracy for computational efficiency. In (Hutangkabodee et al., 2006), the Composite Simpson's Rule and Newton Raphson method are utilized for online determination of terrain parameters from measured forces. In (Ray, 2009), a multi-model approach is used to efficiently select a terrain parameter set from a precompiled library of parameter sets and mappings determined *a priori*. Finally, in (Setterfield and Ellery, 2013) polynomial models representing terrain response are developed from measurements including rover velocities and forces rather than explicitly estimating the terrain parameters, but real-time implementation was not achieved.

While existing results are promising, several limitations of the existing literature are important for this work: (1) linear approximations can lead to inaccurate stress approximations, particularly in terrains with low sinkage exponents such as clay (Zhenzhong Jia et al., 2011), and hence inaccurate force prediction, (2) these algorithms often rely on measurements obtained from force and torque sensors, which are not necessarily standard on AGVs, and (3) periodically operating at low speeds is not desirable when maximum mobility is desired. Hence, online estimation of deformable terrain parameters for off-road AGVs is still an open research area and is the focus of this work.

This study presents a new approach for online terrain parameter estimation. First, due to the large computation time associated with integrating stresses in SCM and limitations of classical terramechanics equations, a nonlinear reduced-order model is developed by extending the work presented in (Zhenzhong Jia et al., 2011) to account for additional dynamic effects such that a sufficient agreement with SCM can be achieved. Then, the reduced-order terramechanics model is incorporated in a 3 DoF bicycle model (Liu et al., 2018) to create an estimation model, whereas the actual vehicle is represented with a 11 DoF plant model with SCM or a physical vehicle operating on a grass field. The predictions from the estimation model are fused with measurements from the plant model, independent of forces and torque measurement, in an Unscented Kalman Filter (UKF) to identify the dominant terrain parameter, namely, the sinkage exponent. The result is an online terrain estimation approach that can be used to better inform control and path-planning algorithms for AGVs.

The rest of this paper is organized as follows. Sec. 2 first briefly reviews the SCM model used in the plant model. Then a state-of-the-art fast terramechanics model used as a benchmark is introduced and the significant deviations of its predictions from SCM are demonstrated. This model is then modified to improve its accuracy vis-à-vis SCM, so that a suitable estimation model is obtained. Sec. 3 presents the vehicle models, both the plant model as well as the estimation model. The terrain estimation procedure based on UKF is summarized in Sec. 4. Sec. 5 and Sec 6 give the simulation and experimental conditions. Sec. 7 gives the simulation results, including the accuracy of the estimations and their ability to improve the predictive accuracy of the 3 DoF model, and the experimental results on grass. Finally, Sec. 8 gives the conclusions drawn from this work.

2. Terramechanics Models

2.1. Soil Contact Model (SCM)

This section briefly reviews the terramechanics model adopted in this work to represent the tire-terrain interactions in the plant simulations with high fidelity. This model is also used to evaluate the accuracy of the fast terramechanics models, including a state-of-the-art model and the surrogate model developed in this work. As such, this model serves as the ground truth for the purposes of this work.

The terramechanics model used in this study for generating the lateral tire forces acting on the vehicle is based on the Soil Contact Model (SCM) reported in (Gallina et al., 2014; Krenn and Gibbesch, 2011). Verification of the model can be found in (Krenn and Hirzinger, 2009). The SCM calculates relevant forces and torques acting on a 3 dimensional object in contact with a deformable terrain as summarized below.

The SCM algorithm relies on a discretized mesh of the tire and terrain to search for contact points at the tire-terrain interface. In the contact detection step, the vertices of the tire mesh are projected onto the nearest vertices of the terrain digital elevation map, effectively arranging the contact vertices in individual columns. The sinkage at each vertex can be determined from the minima of each column, assuming the vertex location is a point of sinkage. The effective contact width, b, can then be determined from the footprint's area and contour length (Krenn and Gibbesch, 2011).

Following contact detection, the algorithm calculates the stresses at each contact node of the footprint as follows. The pressure, σ, is expressed as (Bekker, 1962)

$$\sigma = (k_c/b + k_\phi)h^n \tag{1}$$

The shear stress, τ, is expressed as (Janosi et al., 1961)

$$\tau = \tau_{\max}(1 - e^{-j/k}) \tag{2}$$

with $\tau_{\max}$ given as

$$\tau_{\max} = (c + \sigma \tan\phi) \tag{3}$$

In the above expressions h is the sinkage, b is the tire effective width, and j is the shear deformation. The remaining parameters are internal parameters characterizing the terrain as summarized in Table 1. The forces generated at the tire-terrain interface can then be given by integrating the stresses over the

Table 1: SCM terrain parameters.

Parameter	**Symbol**	**Unit**
Cohesive modulus	k_c	N/m^{n+1}
Frictional modulus	k_ϕ	N/m^{n+2}
Sinkage exponent	n	-
Shear deformation modulus	k	m
Cohesion	c	Pa
Angle of internal friction	ϕ	rad

entire contact patch. The above overview is a summary of (Gallina et al., 2014); a more complete discussion is given in (Krenn and Gibbesch, 2011).

SCM is a rather complex model due to the discretizations and integrations involved and may thus not be suitable for real-time parameter identification purposes. It has been shown that the accuracy of SCM is heavily influenced by the discretization resolution (Krenn and Gibbesch, 2011). Furthermore, several SCM operations are of N^2 complexity, where N is the number of grid nodes (Krenn and Gibbesch, 2011). As an example, for a discretization of just 200 total nodes (100 per tire in a bicycle model), the time required by SCM can be around 20 ms (Krenn and Gibbesch, 2011). Furthermore, for the UKF, the estimation method used in this work, 17 sigma points must be generated as discussed in Sec. 4, each calling the terramechanics model twice (once per tire in the bicycle model). Thus the total time spent calculating tire forces can be around 350 ms per a single UKF iteration. Finally, taking into account that many UKF iterations are needed to achieve estimation convergence, a UKF with SCM can be expected to take several minutes to converge, which is impractically long. Therefore, faster terramechanics models are needed.

2.2. State-of-the-Art Fast Terramechanics Model

Much less computationally demanding solutions better suited for online estimation are given by Bekker-based models. These models are again based on

(1)-(3); however, σ, τ, h, and, j are now replaced by functions of the angle of contact, θ. As such, (1)-(3) are rewritten as:

$$\sigma(\theta) = (k_c/b + k_\phi)h(\theta)^n \tag{4}$$

$$\tau(\theta) = \tau_{\max}(1 - e^{-j(\theta)/k}) \tag{5}$$

$$\tau_{\max} = (c + \sigma(\theta)\tan\phi) \tag{6}$$

where $h(\theta)$ is given by

$$h(\theta) = \begin{cases} r(\cos\theta - \cos\theta_{\mathrm{f}}) & \theta_{\mathrm{m}} \leq \theta \leq \theta_{\mathrm{f}} \\ r(\cos\theta_{\mathrm{e}} - \cos\theta_{\mathrm{f}}) & \theta_{\mathrm{r}} \leq \theta \leq \theta_{\mathrm{m}} \end{cases} \tag{7}$$

with

$$\theta_{\mathrm{m}} = (a_0 + a_1 s)\theta_{\mathrm{f}} \tag{8}$$

$$\theta_{\mathrm{f}} = \cos^{-1}(1 - h_f/r) \tag{9}$$

$$\theta_{\mathrm{e}} = \theta_{\mathrm{f}} - (\theta - \theta_{\mathrm{r}})(\theta_{\mathrm{f}} - \theta_{\mathrm{m}})/(\theta_{\mathrm{m}} - \theta_{\mathrm{r}}) \tag{10}$$

$$\theta_{\mathrm{r}} = \cos^{-1}(1 - \Lambda h/r) \tag{11}$$

where r is the radius of the tire; θ_{f} is the angle at which the front of the tire comes into contact with the terrain; θ_{m} is the location of maximum normal stress with a_0 and a_1 as terrain parameters typically taking on values of 0.4 and 0–0.3, respectively (Wong and Reece, 1967); s is the longitudinal slip of the tire; θ_e is the equivalent front contact angle for angles less than θ_m; θ_{r} is the angle at which the rear of the tire loses contact with the terrain; and Λ is a property of the terrain characterizing the sinkage ratio. Note that Λh in (11) corresponds to the h_r in Fig. 1a.

Finally, $j(\theta)$ is given as

$$j(\theta) = \begin{cases} r[(\theta_{\mathrm{f}} - \theta) - (1-s)(\sin\theta_{\mathrm{f}} - \sin\theta)] & s \geq 0 \\ r[(\theta_{\mathrm{f}} - \theta) - (1/(1+s))(\sin\theta_{\mathrm{f}} - \sin\theta)] & s < 0 \end{cases} \tag{12}$$

The maximum sinkage can be calculated in an iterative fashion by using the Newton-Raphson method as proposed in (Guo, 2016) as follows. The maximum sinkage is initialized as the static sinkage, which is based on the load on the tire W:

$$h_0 = \left[\frac{3W}{b(3-n)(k_c/b + k_\phi)\sqrt{2r}} \right]^{\frac{2}{2n+1}} \tag{13}$$

However, due to dynamic effects, such as slippage, additional sinkage is induced. To account for this, the reaction force is calculated as

$$F_z = \int_{\theta_{\mathrm{r}}}^{\theta_{\mathrm{f}}} rb(\tau(\theta)\sin(\theta) + \sigma(\theta)\cos(\theta))d\theta \tag{14}$$

and a new sinkage is determined using the Newton-Raphson root finding method as

$$h_0' = h_0 - F_z(h_0)/F_z'(h_0) \tag{15}$$

where F_z' denotes the derivative of the reaction force with respect to sinkage. The iterative procedure terminates when the calculated reaction force is within a specified tolerance of the normal force applied to the tire. Once the maximum sinkage is determined, the lateral force F_y can then be calculated in a similar fashion as in (Ishigami et al., 2007; Guo, 2016), i.e.,

$$F_y = \int_{\theta_{\mathrm{r}}}^{\theta_{\mathrm{f}}} rb\tau_y(\theta) \tag{16}$$

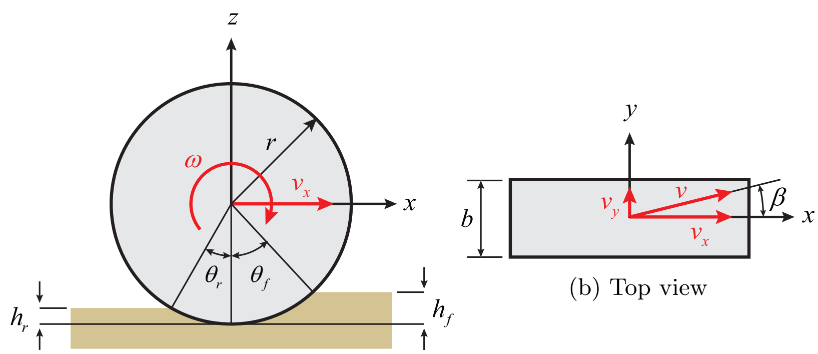

(a) Side view (b) Top view

Figure 1: Tire-terrain geometry for positive slip.

with $\tau_y(\theta)$ given as

$$\tau_y(\theta) = \tau_{\max}(1 - e^{-|j_y(\theta)|/k_y}) \tag{17}$$

where

$$j_y(\theta) = r(1 - s)(\theta_{\mathrm{f}} - \theta)\tan\beta \tag{18}$$

and β is the side slip angle given as

$$\beta = arctan(\frac{v_y}{v_x}) \tag{19}$$

Depending on the soil type $\tau_y(\theta)$ can also be represented with a different formulation such as

$$\tau_y(\theta) = \tau_{\max}(j/k_y)(e^{1-j_y(\theta)/k_y}) \tag{20}$$

Other formulations can be found in (Smith, 2014). All relevant variables are depicted in Fig. 1.

To assess the accuracy of (16) compared to SCM, a simulation is run in Chrono (Tasora et al., 2016). The simulation utilizes a single wheel test bed operating on a sand-like terrain using Chrono's built-in SCM terrain. The test

Table 2: Terrain parameters for sand (Guo, 2016).

Parameter	Value
k_c	1000 (N/m^{n+1})
k_ϕ	1528600 (N/m^{n+2})
n	1.08 (–)
k	0.024 (m)
c	200 (Pa)
ϕ	0.4712 (rad)

Table 3: Wheel states for benchmark simulation.

State	Value
Normal load	2500 (N)
Longitudinal slip	0.2 (–)
Camber angle	0 (rad)
Speed	5.5 (m/s)

bed allows for individual control of the tire's velocity, load, longitudinal slip, and lateral slip. The terrain properties used in this simulation are representative of sand and given in Table 2. The simulation sweeps the tire through a range of lateral slips with a 1 Hz sine wave. The load, longitudinal slip, camber angle, and linear velocity of the tire are all held at the constant values given in Table 3.

Fig. 2 shows the results of an SCM simulation run in Chrono (orange) and the force predicted by (16) (blue). The term k is assumed to be constant, rather than a function of lateral slip as in (Ishigami et al., 2007). This is to maintain consistency with the SCM formulation used in Chrono. As seen in the figure, the base model of (16) captures the overall trend, at least in the linear region around zero lateral slip, but averages the two distinct curves seen in SCM. This is because the current formulation does not account for the hysteresis effects of varying lateral slip; i.e., the shear deformation of (18) does not account for the shearing resulting from the tire rotation that induces the lateral slip. Note that

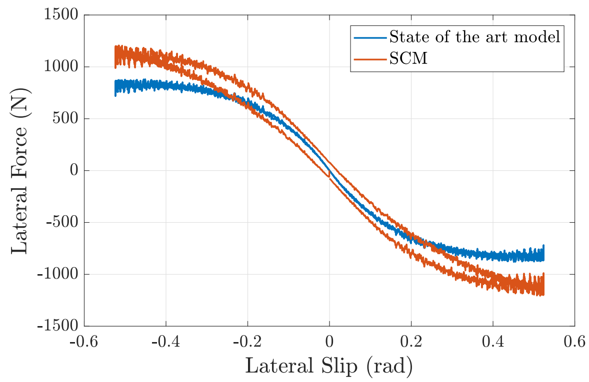

Figure 2: Simulation results for SCM (orange) and model based on (16) (blue). The simulation uses the inputs given in Table 3 and the terrain properties given in Table 2.

in this work the lateral slip is varied by the steering angle applied to the tire.

Recognizing this shortcoming in the state-of-the-art fast terramechanics model, a new surrogate model for SCM is developed in the next section.

2.3. New Surrogate Model

This section presents the new terramechanics model developed as a fast surrogate for the SCM.

The new surrogate is obtained by replacing (17) and (20) with the following expressions, respectively.

$$\tau_y^*(\theta) = \tau_{\max}(1 - e^{-|j_y^*(\theta)|/k_y^*})g_1(v, s, F_z, n) \tag{21}$$

$$\tau_y^*(\theta) = \tau_{\max}(j/k_y^*)(e^{1-j_y^*(\theta)/k_y^*})g_1(v, s, F_z, n) \tag{22}$$

with

$$\begin{aligned} j_y^*(\theta) = &- |r(1-s)(\theta_f - \theta)\tan\beta| + \\ &\operatorname{sign}(\beta)\big(r\sin(\theta)\Delta\delta\, g_2(v, s, F_z, n)\big) \end{aligned} \tag{23}$$

where $\Delta\delta$ is the change in the steering angle. k_y, a parameter originally describing the shear displacement required to generate peak shear stress, is now empirically estimated as a function of the wheel states, i.e.,

$$k_y^* = g_3(v, s, F_z, n) \tag{24}$$

The lateral force acting on the vehicle is then determined as in (16). It should be noted that an additional term in (16) is often given representing the bulldozing force; however, simulations suggest this contribution is minimal for this application. Additionally, integrating the original nonlinear functions over the contact patch is a computationally demanding task. Therefore, the quadratic approximation proposed in (Zhenzhong Jia et al., 2011) is adopted in the surrogate model. Furthermore, the modifications shown represent the lateral force acting on the vehicle frame, not the lateral forces in the tire reference frame.

Simulations covering the operating range of a notional military AGV are run to develop the modifying functions $g_1(\cdot) - g_3(\cdot)$. For each slip range of the clay simulation, as described in the Appendix, the simulations are run at 4 equispaced wheel loads, 5 slips, 5 translational velocities, and 7 sinkage exponents, i.e. 4+5+5+7 samples. It is worth noting, this could potentially cause a loss of interaction effects between the inputs; however, training with 4+5+5+7 samples rather than 4*5*5*7 samples leads to much faster development time. Furthermore, to ensure this method leads minimal loss of accuracy from interaction effects, over 1,500 independent validation tests were performed for cases where interacting effects would occur, as described in the following paragraphs. Finally, other terrain parameters are set to their nominal values, because only the sinkage exponent is selected as the parameter to be estimated due to the higher sensitivity of tire forces to sinkage exponent than other parameters (Gallina et al., 2014; Ishigami, 2008). Table 4 shows the range of inputs covered in the simulations. In these simulations, the inputs are held at constant values

Table 4: Wheel states and terrain ranges for development of $g_1(\cdot) - g_3(\cdot)$

State	**Value**
Normal load	1000–4000 (N)
Longitudinal slip	-0.9–0.9 (–)
Camber angle	0 (rad)
Speed	2.5–8.5 (m/s)
n	0.4–1.3 (–)

and the lateral slip is varied with a sinusoidal input. Following this, correction factors are determined for τ_y, $j_y(\theta)$, and k_y to match the output of (16) with each of the SCM simulations. Least squares curve fitting is then used to derive the relationship between the correction factors and the simulation inputs of Table 4, resulting in the modification functions $g_1(\cdot) - g_3(\cdot)$. To ensure the model was not subject to overfitting or a loss of accuracy from interaction effects, over 1,500 independent validation simulations were performed as described in the following paragraphs.

Several parameters in the surrogate terramechanics model have distinct effects on the lateral force prediction and can be modified to achieve better agreement with SCM. For illustration purposes, the effects of each input on a sand terrain are shown in Fig. 3-5. The slope of the linear region can be set by modifying k_y with $g_3(\cdot)$, the distance between the two curves can be set by adjusting j_y with $g_2(\cdot)$, and the overall magnitude of the force can be adjusted with $g_1(\cdot)$. The effect of the wheel states on $g_1(\cdot) - g_3(\cdot)$ are as follows. The effect of wheel load can be captured with linear functions for $g_1(\cdot) - g_3(\cdot)$. Increased wheel load tends to increase the magnitude of the lateral force, increase the slope of the linear region, and increase the separation between the top and bottom curves as shown in Fig. 3 for a load 2000N (blue) and 3000N (orange). The effect of longitudinal slip can be modeled by polynomials for $g_1(\cdot) - g_3(\cdot)$. As seen in Fig. 4, for positive slips, lower magnitude longitudinal slips tend to increase the

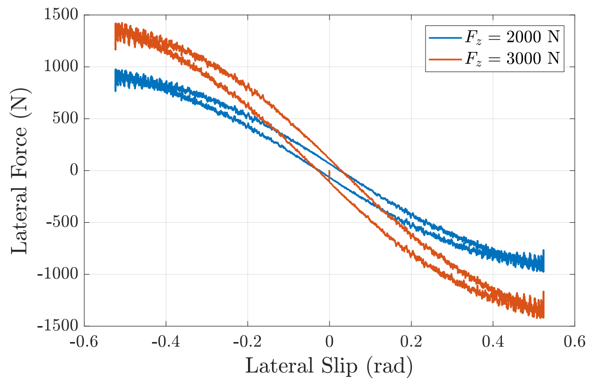

Figure 3: Simulation results for SCM with F_z being 2000 N (blue) and 3000 N (orange). The simulation uses the inputs given in Table 3 and the terrain properties given in Table 2, except for the normal load and slip (-0.5).

slope of the linear region, while also causing a larger spread between the top and bottom curve. Fig. 4 shows these results for a slip of 0.2 (blue), 0.4 (orange), and 0.6 (yellow). The effect of translational velocity can be captured with a power function for $g_2(\cdot)$ alone, because it has minimal effect on $g_1(\cdot)$ and $g_3(\cdot)$. Hence, $g_1(\cdot)$ and $g_3(\cdot)$ do not depend on translational velocity. As seen in Fig. 5, for a speed of 2.5 m/s (blue) and 4.5 m/s (orange), increased translational velocity tends to have little effect on the slope of the linear region, but reduces the hysteresis. Example formulations of $g_1(\cdot) - g_3(\cdot)$ for a clay terrain are given in the Appendix.

Once $g_1(\cdot) - g_3(\cdot)$ are determined, over 1,500 independent validation simulations are ran using equispaced samples for the wheel states of Table 4. The mean absolute error for 1,500 SCM clay simulations is 62.97 N, suggesting the surrogate model is able to accurately predict the tire forces beyond the training set and incurs minimal loss of accuracy from the interaction effects of the training method. The results of the surrogate model are shown in Fig. 6 (blue) while SCM is shown in (orange), for the same SCM simulation of Fig. 2. Much better agreement is observed between the surrogate model and the SCM simulation compared to Fig. 2. It should also be noted that the surrogate model runs in

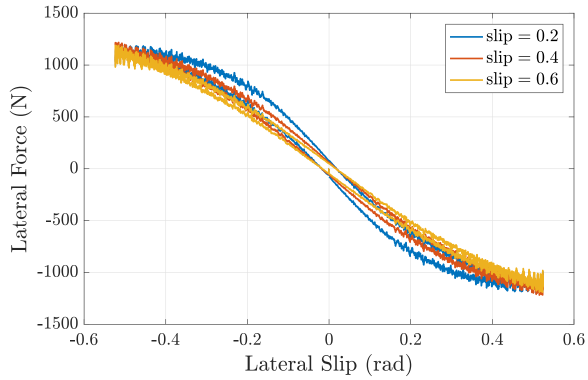

Figure 4: Simulation results for SCM with slip being 0.2 (blue), 0.4 (orange), 0.6 (yellow). The simulation uses the inputs given in Table 3 and the terrain properties given in Table 2, except for the slip.

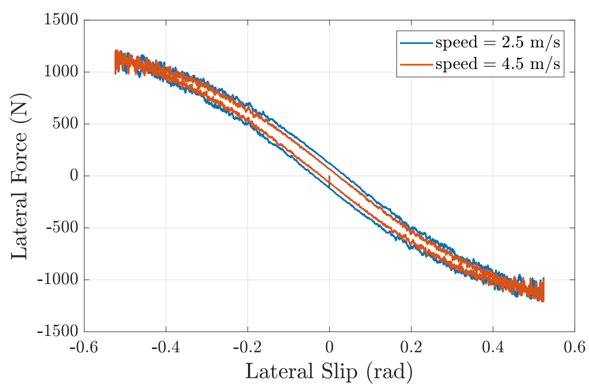

Figure 5: Simulation results for SCM with speed being 2.5 m/s (blue) and 4.5 m/s (orange). The simulation uses the inputs given in Table 3 and the terrain properties given in Table 2, except for the speed and slip (0.5).

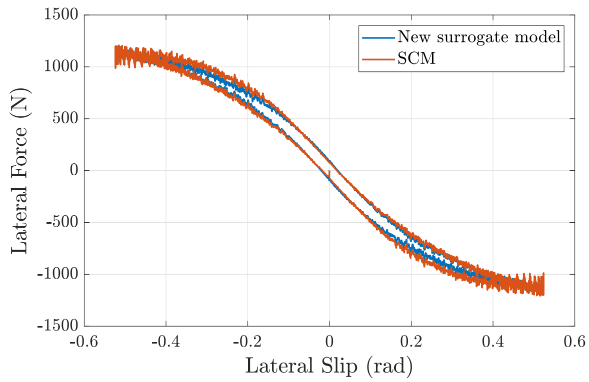

Figure 6: Simulation results for SCM (blue) and the new surrogate model (orange) for the inputs given in Table 3 and the terrain properties given in Table 2.

200-400 μs, which is an order of magnitude more efficient than what is reported for SCM and more suitable for online terrain estimation.

3. Vehicle Models

Two vehicle models are employed in this work; a 11 DoF model to represent the plant and a 3 DoF bicycle model to be used as part of the estimator. This section describes these models.

3.1. Plant Model

To represent the actual vehicle in the simulation-based validation of the proposed surrogate model and terrain estimator, the Chrono software is utilized to simulate the dynamics of a notional military vehicle, specifically a Polaris MRZR 4, as well as to implement the SCM (Tasora et al., 2016). For the purposes of this work, the vehicle is modeled with a double wishbone suspension, rack-pinion steering, 4 wheel drive, and a simple powertrain without a torque converter or transmission. This results in a 11 DoF vehicle model that is then combined with the SCM as the tire-terrain interaction model. Fig.7 depicts the plant operating on a sand SCM terrain in Chrono. The data received from the

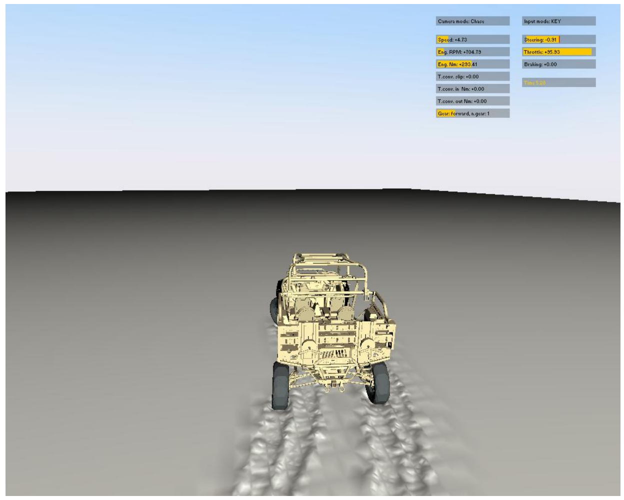

Figure 7: Plant operating on sand SCM terrain in Chrono.

Table 5: Measurement standard deviations used for sensor simulation.

State	**Noise (σ)**
x	1.2 (m)
y	1.2 (m)
ψ	0.0175 (rad)
u	0.25 (m/s)
v	0.25 (m/s)
ω_z	0.0175 (rad/s)

plant is then corrupted with Gaussian noise and serves as the measurement y_k in (29) in Sec. 4. Table 5 lists the standard deviations used in the noise model for each state. Actual sensors typically offer lower noise levels; hence the chosen standard deviations represent a worse-case scenario to test the ability of the estimator (Ryu et al., 2002).

3.2. Bicycle Model

As part of the terrain estimation process that is detailed in Sec. 4, a vehicle model is needed to predict future vehicle states based on the tire forces from the surrogate model. For this work, a 3 DoF bicycle model with forward Euler

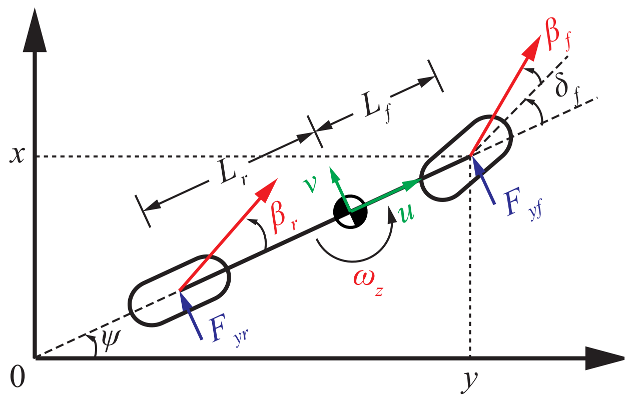

Figure 8: Bicycle model schematic (Liu et al., 2017)

integration is adopted, as it provides a proper level of fidelity while maintaining enough simplicity for short-horizon predictions (Liu et al., 2016). Fig. 8 depicts the bicycle model schematic. Mathematically, the bicycle model takes on the following form:

$$\dot{z_b} = \begin{bmatrix} u\cos\psi - (v + L_{\mathrm{f}}\omega_z)\sin\psi \\ u\sin\psi + (v + L_{\mathrm{f}}\omega_z)\cos\psi \\ w_z \\ a_x \\ (F_{\mathrm{yf}} + F_{\mathrm{yr}})/M_t - u\omega_z \\ (F_{\mathrm{yf}}L_{\mathrm{f}} - F_{\mathrm{yr}}L_{\mathrm{r}})/I_{zz} \end{bmatrix} \tag{25}$$

where the state vector, z_b, is defined as

$$z_b := \begin{bmatrix} x \\ y \\ \psi \\ u \\ v \\ \omega_z \end{bmatrix} = \begin{bmatrix} \text{global } x \text{ position of front axle} \\ \text{global } y \text{ position of front axle} \\ \text{yaw angle} \\ \text{longitudinal velocity} \\ \text{lateral velocity} \\ \text{yaw rate} \end{bmatrix} \tag{26}$$

with M_t being the vehicle mass, I_{zz} being the vehicle's yaw moment of inertia, and L_f and L_r being the distance from the vehicle's center of gravity to the front and rear axles, respectively. Finally, F_yf and F_yr are the lateral forces generated from the front and rear tires acting on the vehicle body, as obtained from the terramechanics model.

4. Terrain Estimation

The terrain parameter to be estimated is chosen as the sinkage exponent n, because it has been shown to be the dominant parameter (Gallina et al., 2014). All other terrain parameters are assumed to be some nominal values based on the specific terrain type, which can be determined from terrain classification algorithms such as the ones described in (Iagnemma, 2006; Weiss et al., 2008).

To estimate the unknown terrain parameter n, it is appended to the 3 DoF bicycle model in (25) with trivial dynamics. Here n is given as a 2x1 vector to account for the front and rear tires. This is to mitigate the influence of unmodeled multipass effects and in the case of a discrete terrain change where the front tire and rear tire may operate on different terrains. The augmented state vector and state dynamics are given as

$$z := \begin{bmatrix} z_b \\ n \end{bmatrix}, \quad \dot{z} = \begin{bmatrix} \dot{z}_b \\ 0 \end{bmatrix} \tag{27}$$

Given the measurements of the vehicle states in (26), the augmented dynamics are utilized in an unscented Kalman filter (UKF) to estimate the augmented state vector in (27) including the sinkage exponent. It is worth noting that many other algorithms are available in the literature for nonlinear parameter estimation, including, but not limited to, extended Kalman filters, transitional Markov Chain Monte Carlo algorithms, and particle filters. Among these options the UKF is preferred in this work, because preliminary explorations suggest that the UKF offers a good balance between accuracy and computational speed for this application.

The UKF is composed of two general steps; a time update step and a measurement update step. Assume that a system is given in discrete time as:

$$z_{k+1} = F(z_k, \rho_k) \tag{28}$$

$$y_k = H(z_k, \gamma_k) \tag{29}$$

where z is the state, y is the observation, and ρ and γ are the process and observation noise, respectively. The functions $F(\cdot)$ and $H(\cdot)$ are nonlinear functions describing the dynamics and outputs. In this application, z takes the form of the state vector in (27) and $F(\cdot)$ is obtained by discretizing the state equation in (27) using the forward Euler method. $H(\cdot)$ is given as the state vector in (26).

First, a set of $2L + 1$ sigma points are created to capture the statistical distribution of the states, where L is the dimension of the state vector z. The sigma points are determined as follows:

$$Z_{k-1} = [\hat{z} \quad \hat{z} \pm (\sqrt{(L+\lambda)P_z})_i] \tag{30}$$

where $\hat{z}$ is the mean value of z. λ is a scaling parameter given as:

$$\lambda = \alpha^2(L+\kappa) - L \tag{31}$$

where α is a tunable scaling parameter that typically takes a value between 0 and 1, κ is another scaling parameter that is typically set to 0. At the time update step, the sigma points are propagated through the original nonlinear system as:

$$Z^z_{k|k-1} = F(Z^z_{k-1}, Z^v_{k-1}) \tag{32}$$

The following weights are then calculated

$$W^m_0 = \lambda/(L+\lambda) \tag{33}$$

$$W^c_0 = \lambda/(L+\lambda) + (1-\alpha^2+\zeta) \tag{34}$$

$$W^{m,c}_i = 1/(2(L+\lambda)) \tag{35}$$

where ζ is set to 2 for Gaussian distributions. The statistics of the time update step are then given by:

$$\hat{z}^-_k = \sum_{i=0}^{2L} W^m_i Z^z_{i,k|k-1} \tag{36}$$

$$P^-_k = \sum_{i=0}^{2L} W^c_i (Z^z_{i,k|k-1} - \hat{z}^-_k)(Z^z_{i,k|k-1} - \hat{z}^-_k)^T \tag{37}$$

$$Y_{k|k-1} = H(Z^z_{k|k-1}, Z^n_{k-1}) \tag{38}$$

$$\hat{y}_k^- = \sum_{i=0}^{2L} W_i^m Y_{i,k|k-1} \tag{39}$$

Finally, the measurement update step is given by the following set of equations:

$$P_{\hat{y}_k \hat{y}_k} = \sum_{i=0}^{2L} W_i^c (Y_{i,k|k-1} - \hat{y}_k^-)(Y_{i,k|k-1} - \hat{y}_k^-)^T \tag{40}$$

$$P_{z_k y_k} = \sum_{i=0}^{2L} W_i^c (Z_{i,k|k-1} - \hat{z}_k^-)(Y_{i,k|k-1} - \hat{y}_k^-)^T \tag{41}$$

$$K = P_{z_k y_k} P_{\hat{y}_k \hat{y}_k}^{-1} \tag{42}$$

$$\hat{z}_k = \hat{z}_k^- + K(y_k - \hat{y}_k^-) \tag{43}$$

$$P_k = P_k^- - K P_{\hat{y}_k \hat{y}_k} K^T \tag{44}$$

The above process is a summary of the algorithm given in (Wan and Van Der Merwe, 2000). Intuitively, the process works by merging model-based predictions of the states with their measurements from the plant by exploiting the uncertainties associated with each to determine the best estimates of the states. For further discussion of UKF and details of its implementation, the reader is referred to (Wan and Van Der Merwe, 2000; Kolås et al., 2009). It also worth noting that while this work only focuses on estimating the dominant parameter n, other terrain parameters could be estimated simultaneously, as well. However, this would incur additional computational costs as the state space dimension increases, thus increasing the number of sigma points necessary in the UKF.

5. Simulation Setup

Simulations are performed utilizing Chrono's SCM deformable terrain and the developed AGV model in Sec. 3.1. Two terrains are considered including

Table 6: Terrain parameters for simulated terrains (Smith, 2014).

Parameter	**Sandy Loam**	**Clay**
k_c	5300 (N/m^{n+1})	13200 (N/m^{n+1})
k_ϕ	1515000 (N/m^{n+2})	692200 (N/m^{n+2})
n	0.7 (–)	0.5 (–)
k	0.025 (m)	0.01 (m)
c	1700 (Pa)	4140 (Pa)
ϕ	0.5061 (rad)	0.2269 (rad)

sandy loam and clay. Relevant terrain parameters are given in Table 6. The simulation subjects the AGV to sinusoidal steering commands, steering fully to the left and right over a three second period. The throttle is also varied with a sinusoidal command such that varying speeds are achieved. No braking command is given. The applied steering and speed profiles for the clay simulation are shown in Fig. 9. Throttle and steering commands of the same frequency are given in the sandy loam simulation, as well. Two remarks are in order. First, as seen in Fig. 9, no requirement on constraining the vehicle to low speeds (on the order of 10 cm/s) is made, which is in contrast to previous efforts (Iagnemma et al., 2004). This enables enhanced mobility, which is critical for military applications. Second, a sinusoidal steering input is selected to induce lateral dynamics for the vehicle. Since the bicycle model only utilizes the lateral forces acting on the vehicle, it is critical for the estimation that the vehicle operates in such a way that lateral dynamics are induced. Otherwise, the lack of information on the lateral dynamics leads to parameter variations having negligible effects on the output of the bicycle model. In other words, if F_{yf} and F_{yr} are zero, it is not possible to estimate terrain parameters based on lateral forces. If estimation is required in such a scenario, additional measurement should be exploited.

In all simulations, the simulation time step is set to 2 ms in Chrono. The purpose of these simulations is to determine the estimation algorithm's accuracy and utility under different terrain conditions. Once the simulations are com-

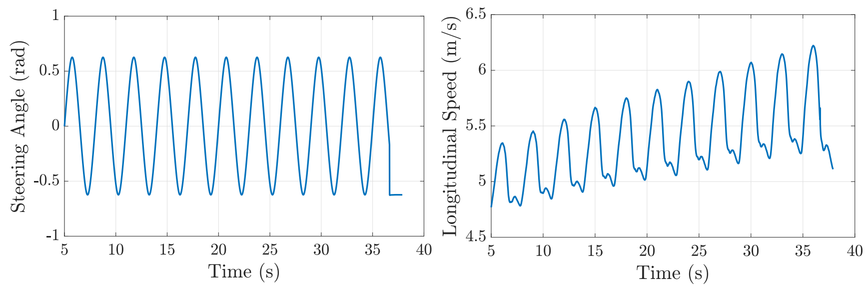

(a) Steering (b) Longitudinal speed

Figure 9: Steering and velocity profiles used in simulation.

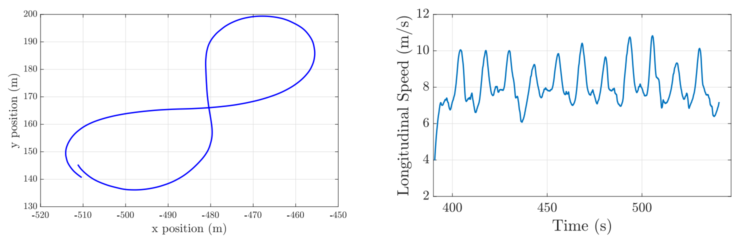

(a) Figure 8 positions. (b) Longitudinal speed

Figure 10: Position and velocity profiles from the experiment on grass.

plete, noise is added to the outputs to simulate sensors, as discussed in Sec. 3.1. The estimator is then run at a 12 ms time step and the simulated measurements are received at every 24 ms. The terrain parameter n is initialized with a value off of the true terrain parameter used in the plant simulation. The remaining terrain parameters are set to their true values given in Table 6. Note that the true values are used here only to assess how closely the algorithm can converge to the true sinkage exponent.

6. Experimental Setup

Experiments were performed with a Polaris MRZR 4, example shown in Fig. 11, equipped with sensors to measure the relevant states required for the measurement update of the UKF as described in Sec. 4. Actuators were con-

Figure 11: Example Polaris MRZR 4 (dvidshub, accessed January 30, 2020).

Table 7: Terrain parameters for grass field (Okello et al., 1998).

Parameter	**Value**
k_c	16000 (N/m^{n+1})
k_ϕ	1180000 (N/m^{n+2})
n	0.26 (–)
k_w	0.046 (m)
c	24000 (Pa)
ϕ	0.75 (rad)

trolled with TORC ByWire, Actus ERC 722 for throttle and braking, and Allied Motion GLOBE POW-R STEER Electric Power Assisted Steering (EPAS) for steering. A Robotic Research RR-N140 navigation system was used for high accuracy localization which is composed of Global Navigation Satellite System (GNSS)/Global Positioning System (GPS) as well as an Inertial Measurement Unit (IMU). In addition, Honeywell SNDH-T4L-G01 were used for wheel encoders. Sensor noise values are given in Table 5. Measurements were received by the UKF at a frequency of 25 Hz and the bicycle model predictions were made at a frequency of 50 Hz.

The vehicle was subjected to a series of Figure 8 maneuvers as exemplified in Fig. 10 (a) with a longitudinal velocity profile given in 10 (b). This maneuver was selected to induce lateral dynamics. The location of the maneuver was a wet open grass field. While the exact terrain parameters of the field are unknown, the literature provides several parameter sets for various grass terrains (Okello et al., 1998). The terrain parameters found in the literature for a terrain most comparable to the test site were chosen as shown in Table 7 due to the moisture content and surface type.

7. Results and Discussion

7.1. Simulation Results

In this section the performance of the terrain estimator is evaluated. The performance is evaluated from two different points of view: (1) the accuracy of the estimated sinkage exponent n, and (2) the accuracy of the predicted state trajectories of the vehicle . The former assesses the algorithm's ability to find the true sinkage exponent, whereas the latter assesses the utility of estimating the sinkage exponent in the larger picture of predicting the future states of the vehicle. Note that if the assumed nominal values for the non-estimated parameters are not representative of the true terrain type, then the estimator may not necessarily converge to the true terrain parameter, as it will attempt to find a value that compensates for the errors in the non-estimated values and achieves the best prediction capability of the vehicle model. For the ultimate aim of more accurately predicting the future mobility capabilities of the vehicle, the second evaluation criterion is the more relevant one.

Table 8 displays the initial guess of the value of the sinkage exponent n, its converged estimate by the algorithm, and the error associated with the estimated parameter. The initial terrain parameter for sandy loam is chosen to be representative of Buchele (Michigan) sandy loam and the initial terrain parameter for clay is chosen to be representative of Thailand clay (Wong, 2001). On both terrains, the percent error in the estimated terrain parameter is less than 4%, where the estimated value is taken to be the final value by the end of the simulation. Fig. 12 shows the estimated terrain parameters for the two

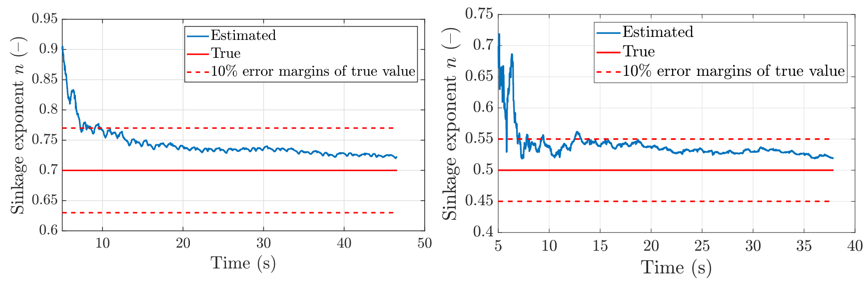

(a) Sandy loam

(b) Clay

Figure 12: Simulated sinkage exponent estimation results.

Table 8: Initial guess, estimated value, and estimation errors of the sinkage exponent n for simulated terrains.

Terrain	**Initial guess**	**True val.**	**Converged val.**	**% error**
Sandy loam	0.9	0.7	0.722	3.1%
Clay	0.7	0.5	0.519	3.8%

considered terrains as time evolves. The differences between the converged and true terrain values can be due to model discrepancies between the high fidelity Chrono model and the 3 DoF bicycle model along with discrepancies arising from the reduced order terramechanics model. Nevertheless, the estimator converges within 10% of the estimated parameter within 5 seconds for both cases.

The peak computation time of the estimator is 10.5 ms and 7.5 ms for clay and sandy loam simulations respectively, thus demonstrating the potential to achieve real-time estimation. The platform running this estimation consists of 16 GB Memory and a single core 3 GHz Intel Core i7 processor.

While estimating the terrain properties accurately is a worthy goal in and of itself, it is more of interest to evaluate to what extent the estimations can improve the predictive capability of the bicycle model as motivated above. To accomplish this second evaluation, the bicycle model, with the terramechanics model parameterized by either the initial guess or the converged terrain parameter, is used to predict the vehicle states approximately 0.5, 2.5, and 5.0 seconds

Table 9: Mean squared error over entire simulation with varying prediction horizons for clay using estimated terrain parameter ($n = 0.519$) and initial guess ($n = 0.7$).

Time horizon	**0.5 (s)**		**2.5 (s)**		**5 (s)**	
State	**n=0.519**	**n=0.7**	**n=0.519**	**n=0.7**	**n=0.519**	**n=0.7**
x (m)	0.0034	0.0025	0.037	0.01	0.075	0.078
y (m)	0.0035	0.0051	0.022	0.15	0.12	0.34
ψ (rad)	3.17e-05	1.8e-04	2.45e-04	0.0089	9.9e-04	0.0115
u (m/s)	6.46e-05	6.46e-05	1.33e-04	1.33e-04	1.2e-04	1.2e-04
v (m/s)	0.0027	0.013	0.0047	0.15	0.005	0.28
ω_z (rad/s)	6.2e-04	0.004 (rad/s)	9.01e-04	0.023	9.05e-04	0.04

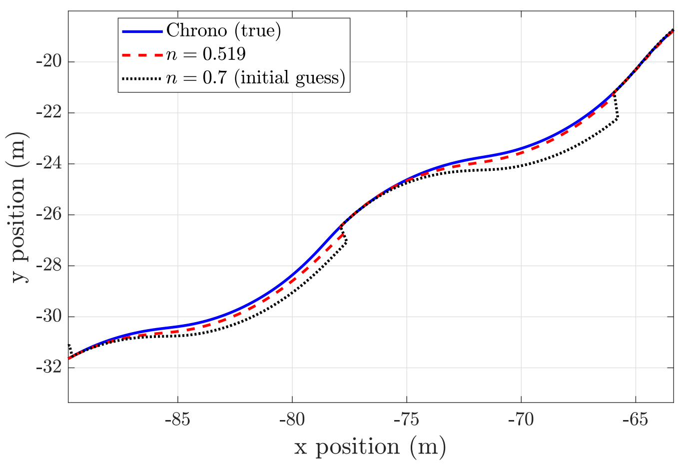

Figure 13: Simulated vehicle positions for AGV operating on clay. True vehicle positions from Chrono (blue solid line), bicycle model parameterized by $n = 0.519$ (red dashed line), and bicycle model parameterized by initial terrain guess $n = 0.7$ (black dotted line).

into the future for the clay case. After this time the vehicle states are reset to the true values received from Chrono. As such, this procedure mimics the operational procedure of a model predictive control approach, where a receding finite horizon optimal control problem is solved periodically with updated information available from sensors (Liu et al., 2017).

Table 9 depicts the mean squared errors (MSE) of the state estimates given by the 3 DoF bicycle model for both the case when the initial guess for the sinkage exponent for clay is used and the case when the converged estimate

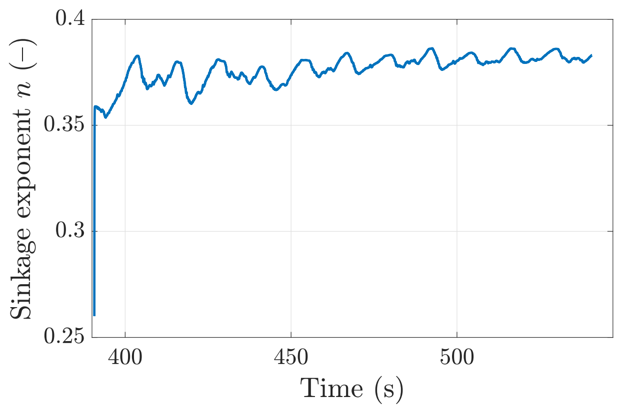

Figure 14: Sinkage exponent estimation results for the experiment on grass.

is used over the entire 32.89 s simulation. The model parameterized by the estimated terrain property yields significantly better predictions, especially at larger time horizons with order of magnitude reductions in MSE. Fig. 13 shows a portion of the simulation, using the ∼2.5s time horizon and depicting the true vehicle positions from the plant (blue solid line), and the predicted positions using the bicycle model with the initial guess of the sinkage exponent (black dotted line) and with the converged sinkage exponent (red dashed line). As can be seen, the converged value yields much more accurate predictions, thus demonstrating the ability of the estimator to significantly improve prediction fidelity. Similar results are also observed for the other terrains, but they are not reported here due to space limitations. This improvement in turn could lead to better performance in model predictive controllers, which is subject to future research.

7.2. Experimental Results

Fig. 14 shows the estimated sinkage exponent for the experimental tests on grass described in Sec. 6. Here, the initial guess of the sinkage exponent corresponds to that of Table 7 and all other terrain parameters are set to nominal

Table 10: Mean squared error over entire experiment with 2.5 second prediction horizon for the experiment on grass.

State	**n=0.39 (estimated value)**	**n=0.26 (initial guess)**
x	0.3132 (m)	1.7305 (m)
y	0.4378 (m)	1.6483 (m)
ψ	0.0117 (rad)	0.0209 (rad)
u	1.8747e-04 (m/s)	1.8747e-04 (m/s)
v	0.1740 (m/s)	0.3989 (m/s)
ω_z	0.0100 (rad/s)	0.0204 (rad/s)

values given in Table 7. While the true sinkage exponent of the grass test site is unknown, the converged value of 0.39 is within the range reported for grass of 0.26-0.7 as given in (Okello et al., 1998).

Table 10 displays the MSE of the state predictions of a 3 DoF bicycle model parameterized by the initial sinkage exponent guess ($n = 0.26$) and the converged estimate ($n = 0.39$) as compared to measurements on the experimental vehicle over a 2.5 s horizon. As can be seen, the model parameterized by the estimate significantly reduces the MSE for all states, demonstrating the utility of estimator. Furthermore, this result provides confidence in the estimated parameter value despite uncertainty in its true value. This is demonstrated by Fig. 15, which plots the normalized sum squared error (SSE) over the entire experiment between a bicycle model prediction (one time step into the future) as compared to state measurements from the vehicle as a function of the sinakge exponent. As can be seen, the sinkage exponent that minimizes this error is approximately 0.395, which is within 1.5% of the estimated parameter value. Thus the experimental results demonstrate the ability of the estimator to improve the prediction capabilities of the bicycle model, which could prove beneficial in model predictive navigation strategies.

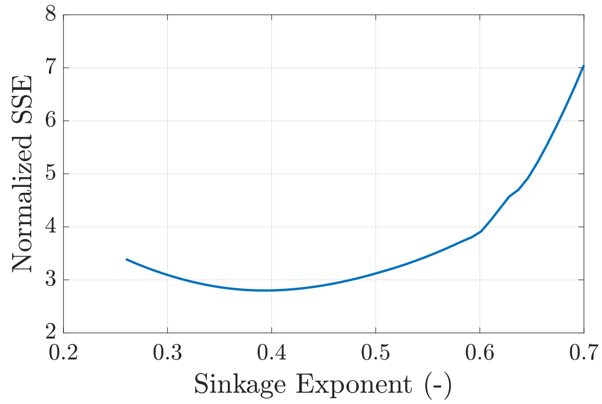

Figure 15: Normalized sum squared error predictions for various sinkage exponents for the experiment on grass.

7.3. Remarks

While the results of the estimator are promising, there are two limiting assumptions of the proposed scheme. The first is that the estimator assumes the terrain is homogeneous. This is common among the approaches reported in the literature (Iagnemma et al., 2004). However, in reality, terrain parameters may be changing and evaluating the performance of the estimator in this scenario is subject to future work. The second limiting assumption is that SCM is treated as the ground truth and the surrogate terramechanics model is parameterized accordingly. The reality may be different than SCM. For example, SCM was originally developed for rover applications which tend to occur at lower speeds. At high speeds, inertial effects may impact model fidelity. However, in that case, a similar procedure in developing the surrogate model could potentially be used by replacing the SCM simulations with an experimental single wheel test bed. While the experimental results presented herein suggest the estimator is able to improve the prediction capability of the bicycle model despite this second limitation, it is still of interest to experimentally validate the developed terramechanics model, which is subject to future work.

8. Conclusion

This paper considers AGVs operating on deformable terrains with unknown terrain properties and develops a novel terrain estimation framework towards increasing the terrain-awareness of the AGV. In particular, the novelty of the framework is the development of a new surrogate terramechanics model for SCM and its use in conjunction with a bicycle model in a UKF. The results suggest that this new framework can estimate the dominant terrain parameter, namely the sinkage exponent, with high accuracy and high computational efficiency. It is therefore concluded that the framework is an important step towards achieving a good balance between estimation accuracy and computational speed. The results also show that the increase in the accuracy of the terrain parameter due to the developed estimation framework leads to a significant increase in the predictive accuracy of the bicycle model, especially for longer prediction time horizons. It is therefore concluded that the proposed framework could be useful to increase the performance of AGVs when they are controlled with model predictive schemes.

Future work includes evaluating the estimator on varying terrain conditions. The need for and ability of estimating multiple terrain parameters also needs to be investigated. It is also of interest to perform experimental validation of the developed surrogate terramechanics model, and investigate the utility of the estimator in a model predictive control framework for terrain-aware autonomous navigation.

Appendix

The following depicts the formulas for $g_1 - g_3$ for a clay terrain. In this work the equations for $g_1 - g_3$ are determined for four separate slip ranges for better agreement. The slip ranges are:

$$0.16 \leq s \tag{45}$$

$$0 \leq s < 0.16 \tag{46}$$

$$-0.157 < s < 0 \tag{47}$$

$$s \leq -0.157 \tag{48}$$

The dependencies for $g_1 - g_3$ on each input is determined through curve fitting to simulation data as discussed in Sec. 2.3. The below equations are valid for the slip range of $0 \leq s < 0.16$. For the lower curve of Fig. 6, the equations are given as:

$$g_1 = g_{1_n} g_{1_s} \tag{49}$$

$$g_2 = g_{2_n} g_{2_s} g_{2_{F_z}} g_{2_v} \tag{50}$$

$$g_3 = g_{3_n} g_{3_s} g_{3_{F_z}} \tag{51}$$

where

$$\begin{aligned} g_{1_n} = {} & 128.3n^5 - 415.4n^4 + 523.3n^3 \\ & -320n^2 + 95.07n - 9.942 \end{aligned} \tag{52}$$

$$\begin{aligned} g_{1_s} = {} & 563.5s^4 - 107.9s^3 - 4.848s^2 \\ & +1.761s + 1.024 \end{aligned} \tag{53}$$

$$g_{2_n} = max(1.8n - 1.08, 0) \tag{54}$$

$$\begin{aligned} g_{2_s} = {} & 1.367 \times 10^6 s^4 - 3.71 \times 10^5 s^3 \\ & +2.809 \times 10^4 s^2 - 545.7s + 70 \end{aligned} \tag{55}$$

$$g_{2_{F_z}} = (0.0001F_z + 0.7) \tag{56}$$

$$g_{2_v} = (4.908v^{-0.9295}) \tag{57}$$

$$g_{3_n} = -0.1235n^2 + 0.7287n + 0.08425 \tag{58}$$

$$\begin{aligned} g_{3_s} = -309.5s^4 + 90.48s^3 - 8.983s^2 \\ +0.2631s + 0.086 \end{aligned} \tag{59}$$

$$g_{3_{F_z}} = (8.3 \times 10^{-5})F_z + 0.76 \tag{60}$$

The same process yields the following equations for the upper curve of Fig. 6

$$g_1 = g_{1_s} \tag{61}$$

$$g_2 = g_{2_n} g_{2_s} g_{2_{F_z}} g_{2_v} \tag{62}$$

$$g_3 = g_{3_n} g_{3_s} g_{3_{F_z}} \tag{63}$$

where

$$\begin{aligned} g_{1_s} = 1.16(1913s^4 - 520.6s^3 + 49.57s^2 \\ -1.204s + 1.024) \end{aligned} \tag{64}$$

$$g_{2_n} = max(1.8n - 1.08, 0) \tag{65}$$

$$\begin{aligned} g_{2_s} = 1.367 \times 10^6 s^4 - 3.71 \times 10^5 s^3 + \\ 2.809 \times 10^4 s^2 - 545.7s + 70 \end{aligned} \tag{66}$$

$$g_{2_{F_z}} = (0.0001F_z + 0.7) \tag{67}$$

$$g_{2_v} = (4.908v^{-0.9295}) \tag{68}$$

$$g_{3_n} = -0.22 \tag{69}$$

$$g_{3_s} = 1609s^4 - 529s^3 + 58.88s^2 - 2.467s + 0.082 \tag{70}$$

$$g_{3_{F_z}} = (8.3 \times 10^{-5})F_z + 0.76 \tag{71}$$

The equations for other slip ranges can easily be determined by repeating the curve fitting process on data in those ranges. Furthermore, it should be noted that these particular equations are only valid for the specific tire under consideration. Should these be used for a different tire, for example of different radius, the equations are no longer valid and the process would need to be repeated.

References

Bekker, M.G., 1962. Theory of Land Locomotion. The University of Michigan Press, Ann Arbor, MI.

Ding, L., Gao, H., Liu, Z., Deng, Z., Liu, G., 2015. Identifying mechanical property parameters of planetary soil using in-situ data obtained from exploration rovers. Planetary and Space Science 119, 121 – 136. URL: http://www.sciencedirect.com/science/article/pii/S0032063315002512, doi:https://doi.org/10.1016/j.pss.2015.09.003.

dvidshub, accessed January 30, 2020. Polaris MRZR 4. https://static.dvidshub.net/media/thumbs/photos/1504/1876593/1000w_q95.jpg.

Gallina, A., Krenn, R., Schäfer, B., 2016. On the treatment of soft soil parameter uncertainties in planetary rover mobility simulations. Journal of Terramechanics 63, 33–47. doi:10.1016/J.JTERRA.2015.08.002.

Gallina, A., Krenn, R., Scharringhausen, M., Uhl, T., Schäfer, B., 2014. Parameter Identification of a Planetary Rover Wheel-Soil Contact Model via a

Bayesian Approach. Journal of Field Robotics 31, 161–175. doi:10.1002/rob.21480.

Guo, T., 2016. Power Consumption Models for Tracked and Wheeled Small Unmanned Ground Vehicles on Deformable Terrains. Ph.D. thesis. University of Michigan.

Hutangkabodee, S., Zweiri, Y.H., Seneviratne, L.D., Althoefer, K., 2006. Performance prediction of a wheeled vehicle on unknown terrain using identified soil parameters, in: Proceedings 2006 IEEE International Conference on Robotics and Automation, 2006. ICRA 2006., pp. 3356–3361. doi:10.1109/ROBOT.2006.1642214.

Iagnemma, K., 2006. Terrain Estimation Methods For Enhanced Autonomous Rover Mobility, in: Howard, A., Tunstel, E. (Eds.), Intelligence for Space Robotics. TSI Press. chapter 17, p. 425.

Iagnemma, K., Kang, S., Shibly, H., Dubowsky, S., 2004. Online Terrain Parameter Estimation for Wheeled Mobile Robots With Application to Planetary Rovers. IEEE Transactions on Robotics 20, 921–927. doi:10.1109/TRO.2004.829462.

Iagnemma, K.D., Dubowsky, S., 2002. Terrain estimation for high-speed rough-terrain autonomous vehicle navigation, in: Unmanned Ground Vehicle Technology IV, pp. 256–266. doi:10.1117/12.474457.

Ishigami, G., 2008. Terramechanics-based Analysis and Control for Lunar/Planetary Exploration Robots. Ph.D. thesis. Tohoku University.

Ishigami, G., Miwa, A., Nagatani, K., Yoshida, K., 2007. Terramechanics-based model for steering maneuver of planetary exploration rovers on loose soil. Journal of Field Robotics 24, 233–250. doi:10.1002/rob.20187.

Janosi, Z., Hanamoto, B., Ferraris, 1961. The analytical determination of drawbar pull as a function of slip for tracked vehicles in deformable soils, in: International Conference of the Mechanics of Soil-Vehicle Systems, Torino, Italy.

Kolås, S., Foss, B., Schei, T., 2009. Constrained nonlinear state estimation based on the UKF approach. Computers & Chemical Engineering 33, 1386–1401. doi:10.1016/J.COMPCHEMENG.2009.01.012.

Krenn, R., Gibbesch, A., 2011. Soft Soil Contact Modeling Technique for Multi-Body System Simulation. Springer, Berlin, Heidelberg.

Krenn, R., Hirzinger, G., 2009. SCM-a soil contact model for multi-body system simulations, in: European Regional Conference of the International Society for Terrain-Vehicle Systems, Bremen, Germany.

Liu, J., Jayakumar, P., Stein, J.L., Ersal, T., 2016. A study on model fidelity for model predictive control-based obstacle avoidance in high-speed autonomous ground vehicles. Vehicle System Dynamics 54, 1629–1650. doi:10.1080/00423114.2016.1223863.

Liu, J., Jayakumar, P., Stein, J.L., Ersal, T., 2017. Combined speed and steering control in high speed autonomous ground vehicles for obstacle avoidance using model predictive control. IEEE Transactions on Vehicular Technology 66, 8746–8763.

Liu, J., Jayakumar, P., Stein, J.L., Ersal, T., 2018. A nonlinear model predictive control formulation for obstacle avoidance in high-speed autonomous ground vehicles in unstructured environments. Vehicle System Dynamics 56, 853–882. doi:10.1080/00423114.2017.1399209.

Okello, J., Watany, M., Crolla, D., 1998. A Theoretical and Experimental

Investigation of Rubber Track Performance Models. Journal of Agricultural Engineering Research 69, 15–24. doi:10.1006/JAER.1997.0220.

Ray, L.E., 2009. Estimation of terrain forces and parameters for rigid-wheeled vehicles. IEEE Transactions on Robotics 25, 717–726. doi:10.1109/TRO.2009.2018971.

Ryu, J., Rossetter, E.J., Gerdes, J.C., 2002. Vehicle Sideslip and Roll Parameter Estimation using GPS, in: International Symposium on Advanced Vehicle Control, Hiroshima, Japan. pp. 373–380.

Setterfield, T.P., Ellery, A., 2013. Terrain response estimation using an instrumented rocker-bogie mobility system. IEEE Transactions on Robotics 29, 172–188. doi:10.1109/TRO.2012.2223591.

Smith, W.C., 2014. Modeling of Wheel-Soil Interaction for Small Ground Vehicles Operating on Granular Soil. Ph.D. thesis. University of Michigan.

Taheri, S., Sandu, C., Taheri, S., Pinto, E., Gorsich, D., 2015. A technical survey on terramechanics models for tireterrain interaction used in modeling and simulation of wheeled vehicles. Journal of Terramechanics 57, 1–22. doi:10.1016/J.JTERRA.2014.08.003.

Tasora, A., Serban, R., Mazhar, H., Pazouki, A., Melanz, D., Fleischmann, J., Taylor, M., Sugiyama, H., Negrut, D., 2016. Chrono: An Open Source Multiphysics Dynamics Engine, in: International Conference on High Performance Computing in Science and Engineering, pp. 19–49.

Wan, E., Van Der Merwe, R., 2000. The unscented Kalman filter for nonlinear estimation, in: IEEE Adaptive Systems for Signal Processing, Communications, and Control Symposium, pp. 153–158. doi:10.1109/ASSPCC.2000.882463.

Weiss, C., Tamimi, H., Zell, A., 2008. A combination of vision- and vibration-based terrain classification, in: IEEE/RSJ International Conference on Intelligent Robots and Systems, pp. 2204–2209. doi:10.1109/IROS.2008.4650678.

Wong, J.Y., 2001. Theory of Ground Vehicles. John Wiley, Hoboken, New Jersey.

Wong, J.Y., Reece, A., 1967. Prediction of rigid wheel performance based on the analysis of soil-wheel stresses part I. Performance of driven rigid wheels. Journal of Terramechanics 4, 81–98. doi:10.1016/0022-4898(67)90105-X.

Zhenzhong Jia, Smith, W., Huei Peng, 2011. Fast computation of wheel-soil interactions for safe and efficient operation of mobile robots, in: IEEE/RSJ International Conference on Intelligent Robots and Systems, pp. 3004–3010. doi:10.1109/IROS.2011.6094507.